X-57 "Maxwell" High-Lift Propeller Testing and Model Development

Brandon L. Litherland,[1] Nicholas K. Borer,[2] and Nikolas S. Zawodny[3]
NASA Langley Research Center, Hampton, VA, 23681, U.S.A.

NASA's X-57 "Maxwell" distributed electric propulsion flight demonstrator has a high-lift system that includes 12 fixed-pitch high-lift propellers located upstream of the wing leading edge for lift augmentation at low speeds. These high-lift propellers are not required at higher speeds and are folded conformally along the nacelles to reduce drag when not in operation. Aircraft performance models and flight simulations incorporate propeller performance to predict thrust, moments, and power consumption and propeller model accuracy is important in identifying safe operating regimes for this aircraft. Current high-lift propeller performance models have been verified and calibrated against numerous computational fluid dynamics analyses under a variety of flight conditions. We performed a series of full-scale wind tunnel tests at the NASA Langley Research Center Low Speed Aeroacoustic Wind Tunnel to further validate these models, to identify any adverse operating conditions for these propellers, and to assess the accuracy of the facility's new Propeller Test Stand. The results indicate that the models accurately predicted performance and that the right-handed propeller showed lower torque and thrust for a given propeller speed compared to the left-handed version. Acoustic data support these measurements, showing higher tonal noise for the left versus right propeller. We suspect this is due to slight differences in the material properties between the early production (right) and more recent (left) blade sets leading to greater detwisting in the right-handed blades under load. Both propellers demonstrated very stable operation throughout the test including during deployment, stowing, and windmilling. Furthermore, high-speed imagery of the spinning propeller indicated no blade oscillations or instabilities for any test case. We also leveraged these images to analyze the effects of propeller loading on blade detwisting and tip position. Unfortunately, the thrust measurements varied significantly during the test due to cross-loading of the Propeller Test Stand load cell, though trends in the thrust data were still observable. The torque measurement, however, remained very precise for all test points and was used for performance comparisons. As a result of this test, we validated and improved the X-57 high-lift propeller performance models, obtained detailed propeller acoustic data and high-speed imagery, observed the propeller operating safely during a variety of dynamic events, and identified two potentially adverse, low-propeller-speed conditions which will be avoided during normal aircraft operation.

Nomenclature

β_{drive} = local blade twist controlling rake and skew
$\beta_{3/4}$ = blade pitch measured at 3/4 radius
η = propeller efficiency
θ_o = observer angle
θ_c = corrected observer angle
ρ = air density

[1] Aerospace Engineer, Aeronautics Systems Analysis Branch, 1 N. Dryden St. MS 442.
[2] Aerospace Engineer, Aeronautics Systems Analysis Branch, 1 N. Dryden St. MS 442, AIAA Senior Member.
[3] Research Aerospace Engineer, Aeroacoustics Branch, 2 N. Dryden St. MS 461 , AIAA Member

Ψ_o = observer inclination angle
Ω = propeller rotational speed
C_P = power coefficient, $C_P = P/(\rho n^3 D^5)$
C_Q = torque coefficient, $C_Q = Q/(\rho n^2 D^5)$
C_T = thrust coefficient, $C_T = T/(\rho n^2 D^4)$
D = propeller diameter
$F_{x,y,z}$ = load cell force in x, y, or z direction
f = frequency
J = propeller advance ratio
n = propeller revolutions per second
P = power
R = propeller radius
r = local blade radial distance
T = thrust
$T_{x,y,z}$ = load cell torque in x, y, or z direction
V_{ref} = reference landing approach speed
V_{inf} = freestream air speed

I. Introduction and Background

This paper presents background, design characteristics, and results from testing full-scale X-57 high-lift propellers (HLP) in the NASA Langley Research Center Low Speed Aeroacoustic Wind Tunnel (LSAWT). The X-57 has 12 high-lift nacelles, each with a five-bladed high-lift propeller. To inform aircraft flight simulations and provide a basis for aircraft performance predictions, we leveraged several propeller performance models generated from a combination of blade element momentum analyses and computational fluid dynamics (CFD). We performed a series of wind tunnel tests on the high-lift propeller at several conditions to gather performance data that improved our performance models and informed us of any adverse operating conditions that should be avoided in flight.

The X-57 "Maxwell," NASA's first manned X-plane developed in two decades, is a fully electric flight demonstrator vehicle intended to inform standards and regulations related to distributed electric propulsion (DEP) technology and to demonstrate how this technology can dramatically increase cruise efficiency over the baseline aircraft [1]. This efficiency improvement is achieved by sizing the wing to be more efficient in high-speed cruise, rather than for slower speeds used for takeoff and landing, and integrating propellers for beneficial aero-propulsive effects. The aircraft is being tested in a number of phases or "Mods," which started with characterizing a baseline aircraft, the two-engine, gasoline-powered Tecnam P2006T, and will end with a modified aircraft with a much smaller wing and distributed electric propulsion system (Mod IV). The cruise-sized wing area is 58% less than the P2006T wing area as shown in Fig. 1. The smaller, cruise-sized X-57 wing would normally require significantly higher takeoff and approach speeds, but by using a high-lift propeller system in combination with flaps, the aircraft can achieve the same stall speed (with high-lift propellers operating) as the baseline aircraft. The "high-lift propellers" are so named because they are designed to act as high-lift devices at low speeds, rather than as traditional propulsors, by accelerating the air over the wing, thus increasing the local dynamic pressure and lift. At higher flight velocities, the lift augmentation is no longer needed. At these speeds, the high-lift propellers are unpowered and would normally result in a large drag contribution if left deployed and windmilling [2]. Instead, the X-57 high-lift propeller blades fold back into a stowed configuration and are designed such that they conform to the nacelles.

A goal of the X-57 project is to help develop certification standards for emerging electric aircraft markets, which may rely on complex DEP systems. NASA is sharing the aircraft's electric-propulsion-focused design and airworthiness processes with regulators and industry, which will advance certification approaches for aircraft utilizing DEP. Additionally, the X-57 team is using "design drivers" as aspirational goals that "push the envelope" and demonstrate the potential impacts of DEP technologies on aircraft and operations. These design drivers include a fivefold reduction in energy consumption in high-speed cruise as compared to the baseline aircraft, zero in-flight carbon emissions, and flight that is much quieter for communities on the ground.

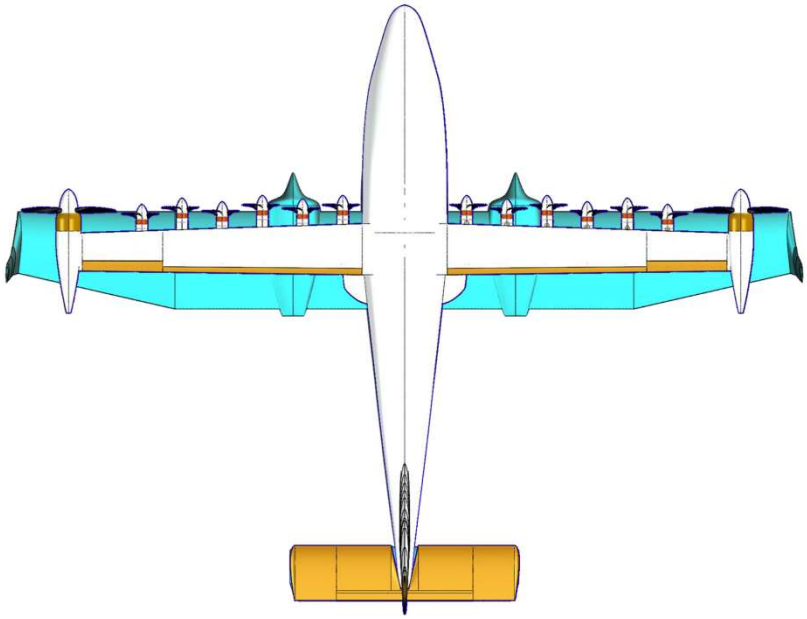

Fig. 1 Top-down view of the X-57 placed on top of the baseline Tecnam P2006T wing.

II. Propeller Design

The X-57 high-lift propeller is designed to produce a relatively constant induced velocity aft of the propeller according to the methods described by Patterson et al. [3]. The propeller root chord was modified from the original design to accommodate folding and stowage along the nacelle by removing material from the leading edge to avoid cutting into the spinner [4]. The blades have a constant MH114 airfoil, which was modified to include a 0.020 inch blunt trailing edge thickness for manufacturability by relofting the airfoil upper surface. Table 1 describes the high-lift propeller dimensions and design flight conditions. The high-lift blades were manufactured by injection molding using a long carbon fiber reinforced polyphthalamide (PPA) thermoplastic composite.

Table 1. High-Lift Propeller Design Parameters

Parameter	Value
Diameter (D)	22.67 in.
Radius (R)	11.34 in.
3/4 Pitch ($\beta_{3/4}$)	27.4°
Number of Blades	5
Speed	4549 RPM
Power (electric)	10.5 kW
Thrust	49.5 lbf
Flight Velocity	58 KTAS, Sea Level

We provide the distribution of chord, twist, rake, and skew along the propeller radius in Fig. 2. Rake and skew are defined relative to the local blade chord[4] as shown in Fig. 3. For example, positive rake is in the direction perpendicular to the local chord line in the airfoil plane and points away from the blade lower surface. Positive skew is in the direction parallel to the local chord line in the airfoil plane and points toward the trailing edge.

[4] Rake and skew differ from dihedral and sweep in that rake and skew are translations relative to the local chord and dihedral and sweep are angular deflections, typically measured at the blade leading edge, relative to the propeller plane of rotation.

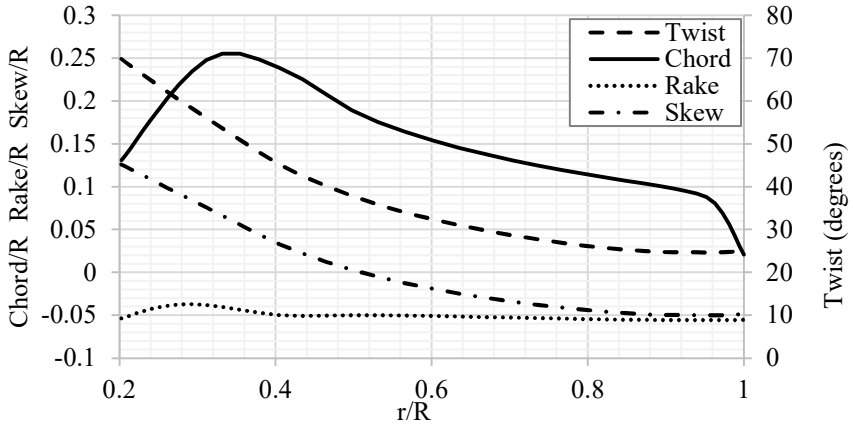

Fig. 2 High-lift propeller blade geometry curves.

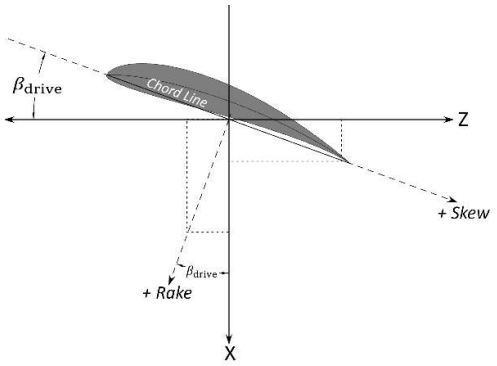

Fig. 3 Rake and skew directions denoted relative to a local blade airfoil section with twist angle of $\boldsymbol{\beta_{drive}}$.

III. Propeller Performance Modeling

In this section, we discuss the tools and methods used to derive the propeller performance model and how this model evolved to capture predicted propeller deployment and operation.

A. Modeling Tools and Methods

1. XROTOR

We performed blade-element momentum (BEM) analyses of the high-lift propeller under a variety of freestream conditions and rotational speeds with XROTOR. XROTOR is a program for the design and analysis of propellers and windmills that consists of several routines performing functions such as designing minimum induced loss propellers, modifying an existing propeller geometry, twist optimization for minimum loss, and propeller analysis under a variety of input parameters [5]. Other useful functions, such as structural analysis, acoustic analysis, geometry and performance plotting, and slipstream analysis, are also included. Patterson leveraged this tool along with custom scripts to create the original, near-constant induced axial velocity propeller design for the X-57 high-lift propeller system [3].

2. OpenVSP

We created the reference propeller geometry and the files needed to export to other tools in Open Vehicle Sketch Pad (OpenVSP). OpenVSP is an open-source, parametric geometry-based computer modeling environment originally funded by NASA [6]. The program enables users to rapidly generate a variety of designs using aircraft-native components, such as wings, fuselages, ducts, and propellers. OpenVSP facilitates the initial creation of conceptual models as well as detailed approximations of existing vehicles and objects. The software includes a variety of analysis

tools: parasitic drag calculators, inviscid flow solvers, mass property computation, and others. OpenVSP can also export geometry in a variety of formats such as IGES, PLOT3D, and STL.

3. Chimera Grid Tools and OVERFLOW

We created the overset grid systems required to perform computational fluid dynamics (CFD) analyses in Chimera Grid Tools (CGT). CGT software contains several pre- and post-processing tools for the Chimera overset approach to gridding for CFD analyses on complex geometries [7].

We performed CFD analyses on the high-lift propeller at various conditions with OVERFLOW (OVERset grid FLOW solver), a structured, overset grid, Reynolds-Averaged Navier-Stokes, CFD flow solver developed at NASA [8, 9]. A fifth-order WENO5M (Weighted Essentially Non-Oscillatory) method [10] with a HLLE++ (Harten, Lax, van Leer and Einfeldt) flux scheme [11] was used to calculate inviscid flux contributions, and second-order central differences were used to approximate the viscous flux. A k-ω SST-RC-QCR2000 (rotation correction with quadratic constitutive relationship) turbulence model [12, 13] coupled with the Langtry-Menter CFX-v-1.1 transition model [14], despite not being Galilean invariant, were used to maintain commonality with previous X-57 studies [1, 4, 2]. This method was successfully demonstrated in other situations with rotational reference frames, e.g., Refs. [15, 16].

4. PTC Creo Parametric

We designed parts and produced drawings for the hardware required to adapt the X-57 high-lift propeller assembly to the Propeller Test Stand using the PTC Creo Parametric computer-aided design (CAD) software [17]. We also performed dynamics simulations of the assembled propeller test rig within PTC Creo Parametric to obtain estimates for the deployed propeller equilibrium position and expected loads. In these simulations, the propeller assembly rotated at the prescribed speed and the expected aerodynamic blade loads were applied at the blade 3/4 span while the blades remained free to rotate about the hinge. Friction and spring restoring forces at the blade hinge were modeled according to the material properties and the spring rate.

B. Propeller Performance Prediction

Dynamics simulations from PTC Creo Parametric predicted approximately a 10° rotation about the hinge axis from fully deployed for the equilibrium position of the blades in the absence of thrust and drag forces at normal propeller rotating speeds. This corresponds to about a -10° coning angle relative to the fully deployed plane of rotation (or 80° deployment from the propeller axis of rotation) as illustrated in Fig. 4. The addition of thrust and drag to these simulations results in varying equilibrium folding angles about the hinge forward from 10° to about 7° at maximum RPM and zero freestream velocity. We chose the 10° equilibrium fold angle as the baseline to be conservative in performance predictions as this produces the largest expected local pitch decrease. At 10°, although the coning angle has a negligible effect on the effective propeller disc diameter, the rotation about the hinge reduces the effective blade pitch by approximately 2.5° to 4.5°, depending on radial location. We calculated the effective blade pitch along the radius based on this configuration (i.e., that shown in in Fig. 4) to create a modified effective high-lift propeller BEM model.

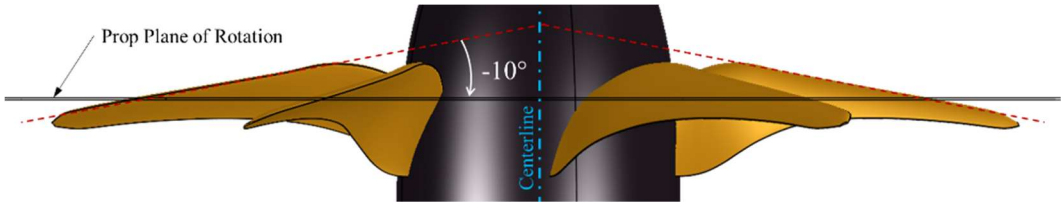

Fig. 4 The predicted equilibrium position of the propeller blades absent thrust and drag.

Borer and Patterson published updated X-57 high-lift propeller control schedules predicted by the modified BEM model which accounts for the expected deployed position of the folding blade at 80° [18]. A comparison between the fully deployed and 80° deployed performance models from this paper is shown in Fig. 5.

The 80° deployed configuration was reanalyzed in OVERFLOW under a limited sweep of advance ratio to compare performance. The modified BEM model shows generally good agreement with OVERFLOW results over the sampled advance ratios with a slight BEM overprediction of thrust (3.1% - 4.6%) and power matching to within 1% on average as shown in Fig. 6.

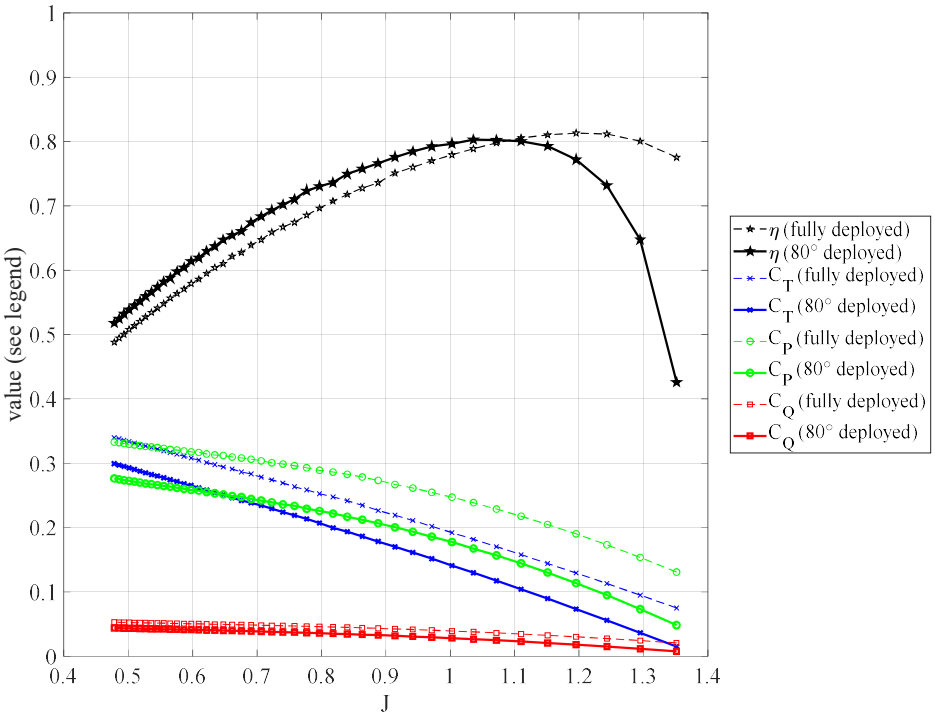

Fig. 5 Comparison of blade-element momentum theory models for the high-lift propeller at full and 80° deployment [18].

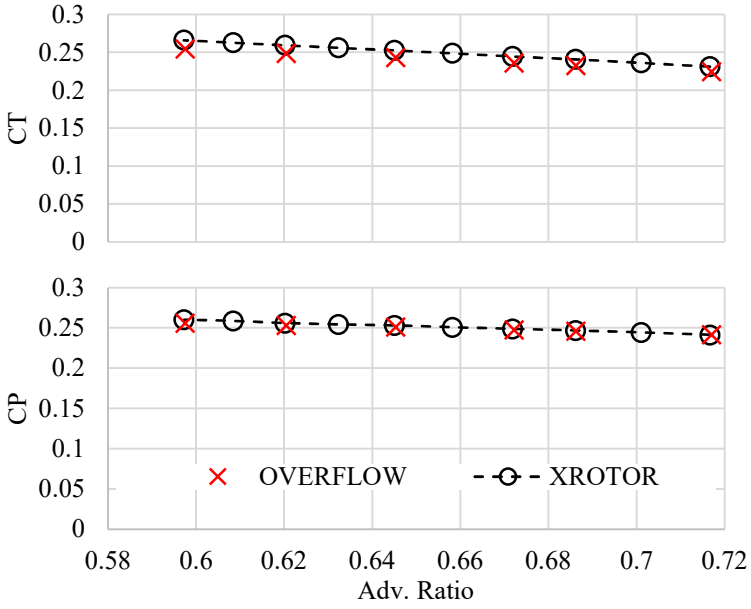

Fig. 6 Comparison of the modified HLP BEM model to OVERFLOW predictions.

IV. Testing Method

A. LSAWT Facility

The Low Speed Aeroacoustic Wind Tunnel (LSAWT) provides forward flight conditions in an anechoic environment for the aeroacoustic testing of propeller and rotor concepts including isolated component, integrated propulsor-airframe, and full-scale small Unmanned Aircraft System (sUAS) vehicle testing for platforms ranging from conventional aircraft to unconventional electric vehicle configurations and UAS. Research objectives in LSAWT tests focus on noise generation processes, investigating complex flow interactions for tool development and validation, and developing effective noise reduction techniques [19]. We provide an illustration of the LSAWT facility layout including the location of the test section in Fig. 7.

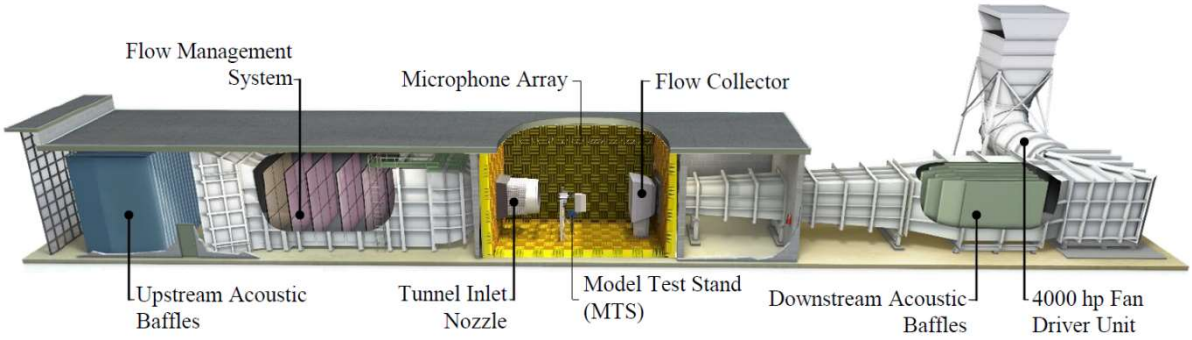

Fig. 7 Facility overview of the flow-through LSAWT including upstream inlets, test section, and fan unit.

B. Propeller Test Stand

The Propeller Test Stand (PTS) was designed for evaluating installed propeller noise and performance in NASA's wind tunnel facilities. The water-cooled drive motor is capable of continuous 52 kW, 15000 RPM operation with an operational speed range of 250 to 16000 RPM. The PTS pitch, roll, and yaw limits are +/- 25.0°, +/- 180°, and +/- 90°, respectively, all to an accuracy of 0.1° with angular rates of 2.6°/sec. Data are relayed to the control and recording station via several devices, including a load cell, accelerometer, and power meter. An illustration of the PTS in the upright position is shown in Fig. 8 [20].

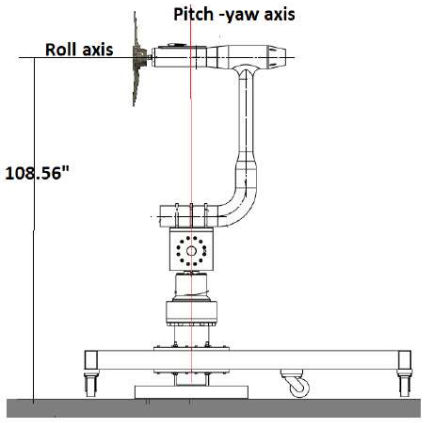

Fig. 8 Side view of the Propeller Test Stand showing propeller ground distance.

C. Measurements

1. *Performance Data*

We acquired propeller performance data from the PTS through a pancake load cell, an aft-mounted accelerometer, and the PTS electrical power cart. The load cell is an ATI Mini85 calibrated to US-105-185 in-lbs range [21]. This load cell is a six-component device that outputs forces and moments about the load cell axes where thrust and shaft torque are in the Z-direction as shown in Fig. 9. Table 2 lists the sensing ranges and resolution for the Mini85 at the US-105-185 calibration used for this test. The accelerometer is a buffered three-axis DE-ACCM3D2 +/- 2 g device with a bandwidth to 500 Hz with 666 mv/g sensitivity powered by a 5 V source [22]. The electrical power for the PTS is supplied by a single, mobile power cart with 480 V, 3-phase input power [20]. Electrical power output data was recorded by sampling the draw through the power cart wiring to the PTS over the duration of each test point.

As shown in Fig. 10, the Mini85 load cell is cross-loaded between the torque, T, and forces, F, in the Z and X/Y directions, and we discovered that a pre-existing side load in the PTS assembly resulted in varying thrust measurements. During high-lift propeller testing we noticed significant drift in the thrust measurements and observed that the drift also correlated with the load cell temperature. This caused a significant amount of uncertainty in the thrust measurements the longer the motor was operated and at higher advance ratios where the propeller was not rotating as quickly. However, the shaft torque measurement remained highly precise and reliable throughout the test. Additional discussion of these effects is provided in section V.B. Performance.

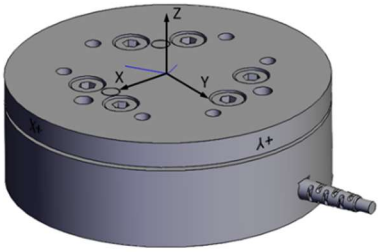

Fig. 9 Rendering of the ATI Mini85 load cell and axes where the Z-axis is forward.

Table 2. ATI Mini85 Load Cell US-105-185 Calibration

Sensing Ranges			
Fx, Fy	**Fz**	**Tx,Ty**	**Tz**
105 lbf	210 lbf	185 lbf-in	185 lbf-in
Resolution			
Fx, Fy	**Fz**	**Tx,Ty**	**Tz**
1/52 lbf	7/260 lbf	5/168 lbf-in	1/48 lbf-in

2. *Acoustic Data*

Acoustic measurements were acquired with a 28-element axial linear array of 6.35 mm-diameter B&K type 4939 microphones [23] positioned along one of the upper corners in the LSAWT test cell. The array is intended to provide a flyover acoustic survey of the article being tested and span an observer angle range of $45° \leq \theta_o \leq 147.5°$. The linear array microphone in closest proximity to the propeller tested in this study is at a radial distance of 138 in. (3.54 m) from the PTS hub. The layout of the LSAWT test section, including the positions and observer angles of the microphone array elements, is shown in Fig. 11.

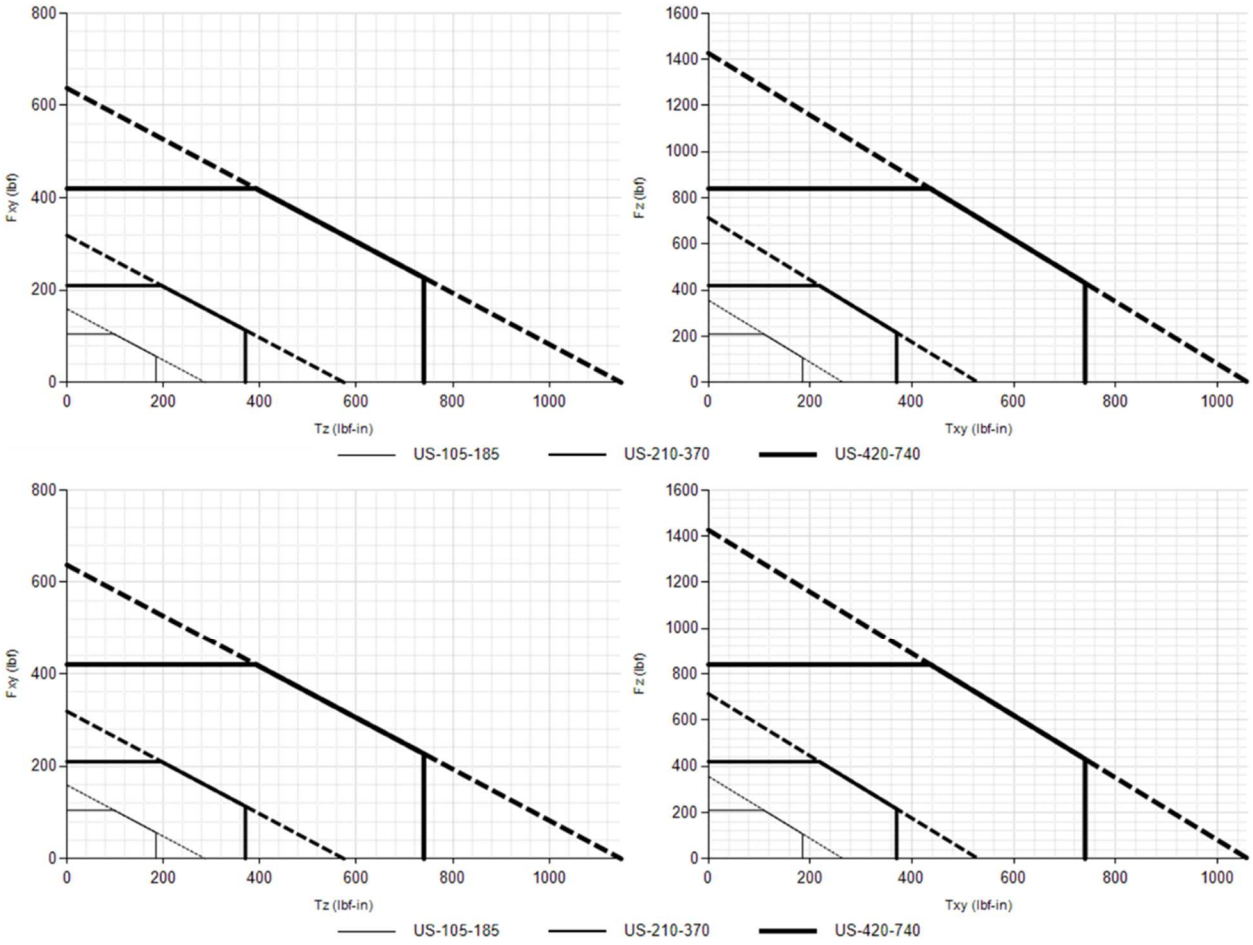

Fig. 10 Complex loading charts for the ATI Mini85 triaxial load cell [21].

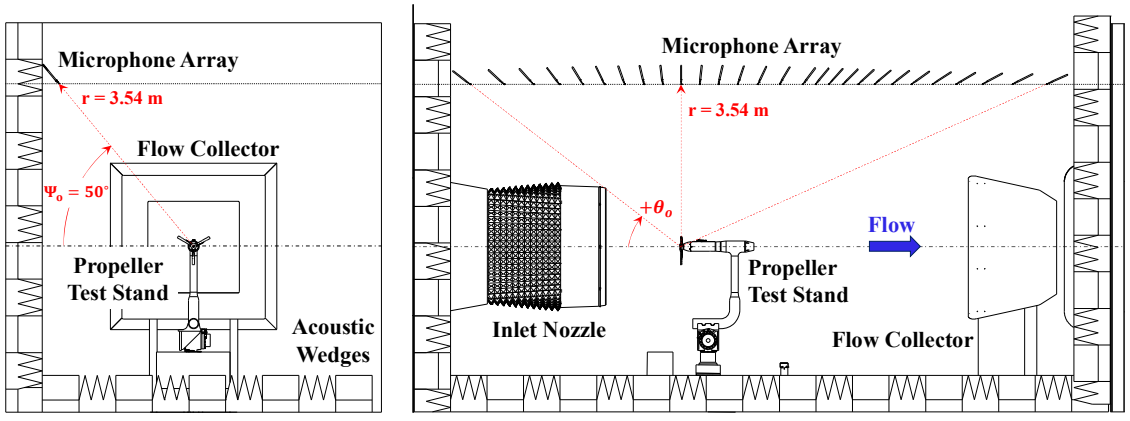

a) Downstream view. **b) Side view.**

Fig. 11 Illustration of LSAWT microphone array and other primary test cell components.

In addition to the linear array, an ACAM 120 [24] commercially available phased microphone array and BeamformX software was also utilized to assist in identifying the location of prominent noise sources (beamforming) on the test rig and in the facility. This array has been found previously to be effective at locating noise sources in the frequency range of $1.5 \leq f \leq 24$ kHz. It is worth noting that the ACAM 120 was positioned in the LSAWT test chamber, outside of the facility flow. Therefore, beamforming results from this array would suffer from shear layer refraction effects. Due to the fact that the BeamformX software does not have a shear layer correction utility included, a slight manual adjustment of convective axial Mach number was applied to approximately account for this slight shift in apparent source location.

3. High-Speed Imagery and Facility Video

Along with performance and acoustic data, we captured high-resolution, high-speed video of the propeller from multiple angles at several test points to evaluate the dynamic behavior of the blades and assembly during operation. An example composite image resulting from the high-speed camera output is provided in Fig. 12. We placed a Vision Research Phantom V12.1 high-speed camera [25] in the forward corner of the test section to capture from an oblique angle to the propeller. We also mounted a Vision Research Phantom V1610 high-speed camera [26] with a 60 mm lens edge-on to the propeller plane of rotation by bolting the camera to a fabricated structure on the PTS that rotated with the stand. We controlled and transferred data between the cameras with Vision Research Phantom Camera Control software (v3.5) through ethernet cables. High-speed imagery was captured at 3000 frames per second with 80 μs exposure per frame on both cameras in raw CINE file format. We also remotely observed the propeller in real-time on the LSAWT facility cameras. The facility cameras provided a side view, oblique forward view, and oblique rear view of the test section while the tunnel was sealed and operating. These cameras provided 60 Hz video feeds to the control room and data acquisition system where the video was time-stamped and recorded. Sample images from the facility cameras are provided in Fig. 13.

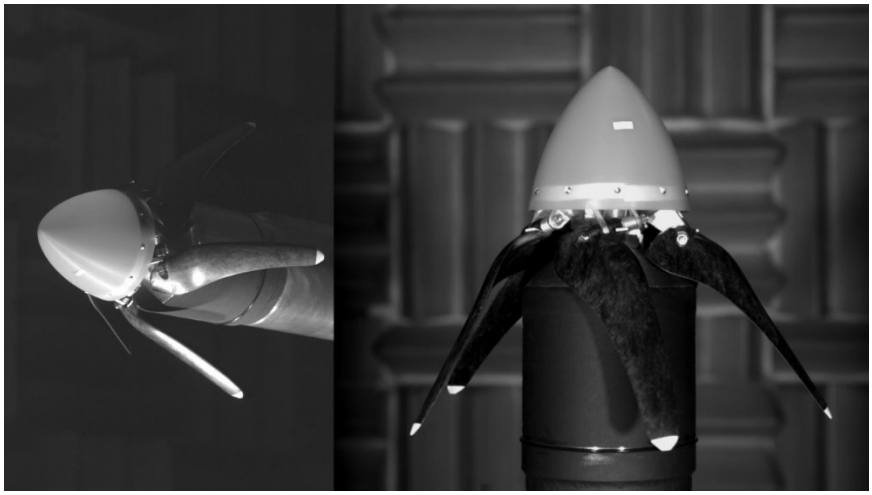

Fig. 12 High-speed camera views from both oblique (left) and edge-on (right) views.

Fig. 13 LSAWT test section camera views from rear corner (left), side wall (middle), forward corner (right).

D. Test Matrix

The test matrix documented in Table 3 shows the various conditions at which data was recorded for the high-lift propeller operating at freestream air speeds, V_{inf}, of 0, 35, 58, 75, and 90 KEAS. Most of these were conducted at zero degrees of angle of attack, though some of the test points involved tests across a range of angles of attack to observe differences in performance or dynamic behavior. The test matrix shown in Table 3 does not show the angle of attack test points since the steady-state results at angle of attack are not summarized in this paper, other than to say that the differences in torque and power were not remarkable. For each range of conditions, we established the tunnel freestream speed prior to activating the propeller. At each test point, we recorded data for a period deemed sufficient to consider the sample "steady" (usually about 12 seconds) while the instruments recorded at prescribed sample rates. We then time-averaged these data to produce a result.

Table 3. Test Matrix for Freestream Speed vs. RPM, Power, or Torque

		Condition																		
		Idle	1500 rpm	2000 rpm	2500 rpm	3000 rpm	3400 rpm	3800 rpm	4200 rpm	4400 rpm	4600 rpm	4800 rpm	5000 rpm	5200 rpm	5400 rpm	5460 rpm	Zero Torque	Max Torque	4.9 kW	10.3 kW
Freestream Speed (KEAS)	0	●	●	●	●	●	●	●	●	●	●	●						●		
	35	●	●	●	●	●	●	●	●	●	●	●					●	●		
	58	●			●	●	●	●	●	●	●	●					●	●		●
	75	●				●	●	●	●	●	●	●					●	●	●	
	90	●						●	●	●	●	●	●	●	●	●	●	●		

Unfortunately, as mentioned before, the Mini85 load cell installed in the PTS experienced significant drift in the thrust measurement, though the propeller shaft torque measurement did not exhibit significant drift. Therefore, we tested at set power or torque conditions, rather than targeting thrust, throughout the range of propeller speeds to compare the performance against the expected values from the model predictions, specifically those corresponding to the high-lift propeller airspeed mode schedule described in Borer and Patterson [18]. For example, the 10.3 kW power condition corresponds to the expected power required to produce 52.4 lbf of thrust at 58 KEAS which represents the high-lift propeller condition at the minimum steady, level flight speed goal of the X-57. The 4.9 kW condition corresponds to the expected power that the high-lift propeller requires according to the airspeed mode schedule at the reference approach speed of 75 KEAS, V_{ref}. The maximum torque setting for the PTS load cell calibration was 195 in-lbs (22 N-m).

We also tested the high-lift propeller while windmilling, i.e., being driven by the freestream air, to evaluate any potential instabilities at this condition. In prior prototype testing [27], the inertia of the windmilling propeller was sufficient to prevent the blades from stowing without applying braking to the motor, and we expected similar behavior in the flight-like assembly even with the inclusion of stowing springs at the blade hinges. However, because the PTS is an RPM-controlled system, which prevents freewheeling the motor, simply commanding a lower RPM than windmilling would not result in the desired response. Therefore, we incrementally decreased the propeller speed until a zero-torque condition was reached, indicating that the motor was neither driving nor being driven by the propeller.

In general, we conducted each series of tests at a particular freestream speed – one row of the test matrix shown in Table 3 for a particular test article (right-hand vs. left-hand), as it was much easier to adjust propeller speed than tunnel conditions. At the conclusion of the tests for a particular freestream speed and test article, we shut down and inspected the propeller prior to the next series of runs. For each test series, each test point was repeated once before moving to the next test point. The test points were selected such that the propeller rotational speed was increased from the lowest desired setting to the highest desired setting, and then reduced again to provide another set of repeating data. We noted significant discrepancies in the thrust measurements in the second half of the test series as we were decreasing from the maximum rotational speed (and motor power). We believe the strong thermal drift noted in the load cell led to this significant change, which had also been observed on the PTS with prior test articles. The torque measurement did not display much drift, indicating that the drift was likely an artifact of the instrumentation, not the test article. As such, many of the results discussed in this paper are related to trends observed in the first half of each test series, in which

the propeller/motor speed is increasing and the motor/load cell combination is heating up, since we believed this set of data to be more accurate. Altogether, we gathered 439 time-averaged data points in over 15 hours of powered operation for the right- and left-hand test articles.

V. Results

This section provides a discussion of the high-lift propeller test results including measurements of the high-lift blade weights, propeller performance and acoustics, and observations from the high-speed video and images.

A. Blade Weights

We weighed and arranged all the high-lift blades on each propeller assembly so that the predicted propeller imbalance side-load at the maximum speed of 5460 RPM would be less than 11.0 lbf. Each blade weight was measured three times on a laboratory scale accurate to +/-0.001 grams and the average of these weights was recorded. Table 4 shows the recorded weights for both right- and left-handed blades. We immediately observed that the right-handed high-lift blades were consistently lighter than the left-handed batch by a small margin. However, because the high-lift blades are very lightweight by design, this small margin reflected a 5.2% average decrease in weight compared to the left-handed average weight. We suspect this difference in weight to be due to the right-handed blades being produced in an earlier batch prior to the left-handed injection mold being fabricated. After thoroughly inspecting the blades for observable defects or physical differences and finding none, we determined that the slightly lower blade weights did not pose a significant risk to test integrity nor did this cause concern about the blade structure.

Table 4. Blade Weights for Right- and Left-Handed High-Lift Propellers

Blade	RH Wt. (oz)	LH Wt. (oz)
1	2.560	2.713
2	2.554	2.689
3	2.576	2.705
4	2.559	2.704
5	2.564	2.701
Average	2.562	2.702
Min	2.554	2.689
Max	2.576	2.713
Delta	0.022	0.024
Min % Diff from Avg.	-0.33%	-0.50%
Max % Diff from Avg.	0.52%	0.39%
Delta % Diff from Avg.	0.85%	0.89%
RH Avg. % Diff from LH Avg.	-5.2%	

B. Performance

1. Propeller Loads

Although the thrust measurements varied significantly among repeated test points as stated previously, the torque remained a reliable indication of propeller performance throughout the test. The plots in Fig. 14 show the thrust and torque coefficients observed across a variety of freestream conditions (58, 75, and 90 KEAS) and test articles (right and left), along with the XROTOR (BEM) predictions for the observed tunnel conditions. As noted earlier, the data summarized here are only shown for the conditions in which propeller rotational speed was increasing from the previous data point, as this was the condition for which the load cell in the thrust direction appeared most accurate (prior to heat-soaking of the load cell at the maximum power point). Even with this filtering, the error estimates (vertical bands) for the thrust coefficient are still significant. For the purposes of this discussion, thrust performance is presented with the understanding that certainty in the measurements is relatively low but that trends in the data may be observed, nevertheless.

Comparisons between the right- and left-handed high-lift propellers are shown in Fig. 14 where we can observe that the right-handed propeller demonstrates diminished performance in both thrust and torque across the range of advance ratios tested. Notice that the right-handed propeller torque is low by a relatively constant offset for most test points except for those where the advance ratio is high, i.e., when the blade is spinning slower and is less heavily loaded. We suspect that this is caused by the right-handed blades being less stiff in bending and torsion than the left-handed blades. In this case, as the aerodynamic and centripetal loads increase, the right-handed blades would tend to

flex and detwist, thus partially unloading the blade. This behavior is further supported by the test points where we fixed the power or torque setting rather than fixing the propeller speed. In each of these tests the right-handed propeller spun at a higher speed for the given setting than the left-handed propeller, even at the zero-torque or windmilling condition. A sample of these test points and the propeller speeds are given in Table 5.

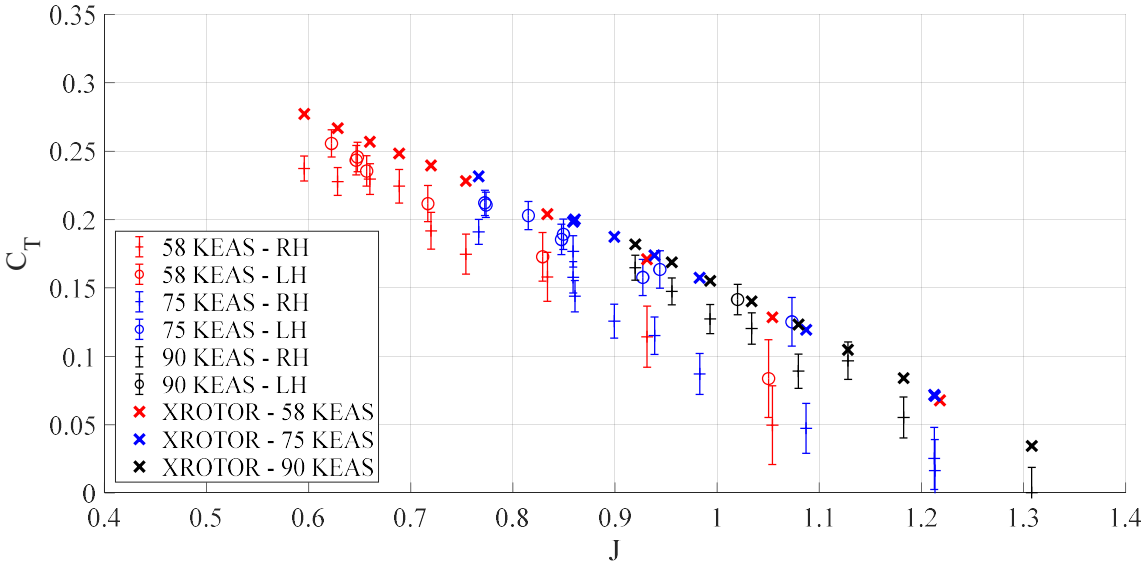

a) Thrust coefficient, C_T

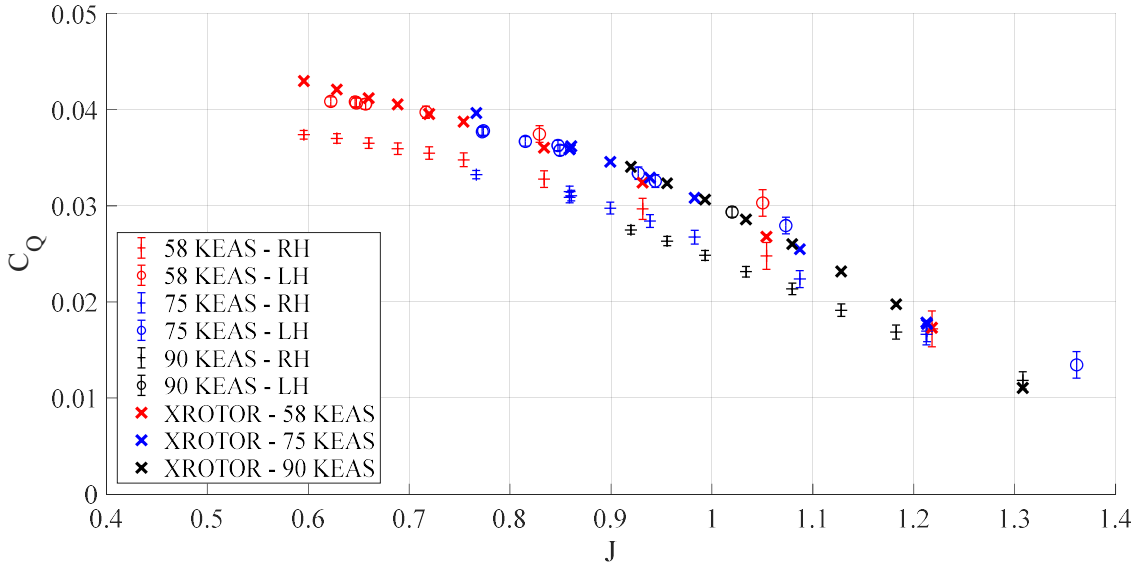

b) Torque coefficient, C_Q

Fig. 14 Comparison between the right-handed and left-handed HLP performance.

We originally believed that the performance discrepancy was likely due to a measurable geometric difference between blade sets, the presence of voids in the injection molded composite, or a difference in the manufacturing conditions leading to a slightly different fill or cure, all of which would present as decreased weight. However, the likelihood of voids in the blade was very low due to the manufacturer's experience with the selected composite and the process of extruding excess material to eliminate these defects. To determine if any geometric differences existed between the two blade sets, we sent the heaviest and lightest blades each from the left and right propellers to the NASA Langley Research Center Quality Assurance laboratory in the Mission Assurance Branch to be laser scanned and then

analyzed against the CAD model. The result of these analyses showed that nearly the entire blade surface from both the left- and right-handed sets matched the CAD geometry to within +/- 0.005 in. with few localized peaks of less than +/- 0.010 in. and were without significant differences in the distribution of these peaks. The test indicated that the blades tested are very nearly identical geometries. Because the hub hinge alignment could also cause differences in the deployed blade orientation, we acquired similar scans and analyses on the two high-lift propeller hubs. These analyses indicated that all five right-handed hub hinge axes deviated angularly from the design intent by no more than 0.5° and that only two of the left-handed axes deviated by more than 0.5° (0.6° and 1.0°). The likely cause of the lower weight and performance in the right-handed propeller is, therefore, a difference in the manufacturing conditions for the earlier batch of right-handed blades.

In contrast, the effective high-lift propeller BEM model seems to have predicted the left-handed propeller performance remarkably well in torque and, arguably, in thrust also. Recall that the modified BEM model demonstrated a very similar overprediction of thrust, on the order of around 4% for advance ratios between 0.6 and 0.7, to the OVERFLOW simulations while power and torque tracked accurately. The agreement with test data along with the correlation to OVERFLOW predictions lend credibility to the modified high-lift propeller BEM model and improve our confidence in the model's ability to predict high-lift propeller performance for the X-57 test flights. With this information, we can easily improve the reference high-lift propeller operating schedule to account for any differences between the predicted thrust or shaft power and the observed test results.

Table 5. Left- vs. Right-Handed Propeller RPM Comparison

Condition	LH	RH	Delta from LH
75 KEAS, Zero-Torque (Windmilling)	2483 RPM	2654 RPM	171 RPM
75 KEAS, 4.9 kW	4152 RPM	4322 RPM	170 RPM
58 KEAS, 10.3 kW	4875 RPM	5045 RPM	170 RPM
75 KEAS, Max Torque	5277 RPM	5396 RPM	119 RPM

2. Propeller Acoustics

The measured differences in blade weights and operational torque between the right- and left-handed blade sets prompted analysis of the measured acoustics from the two propeller blade sets. Due to the relatively thin profile of the blades, the majority of noise generated by the propeller at its design operating condition is due to aerodynamic loading. To illustrate this, an acoustic prediction of the propeller blade passage frequency (BPF) using ANOPP-PAS [28] is provided in Fig. 15 for a high-performance takeoff condition. This condition is selected because it represents one of highest expected propeller rotation rates at the slowest expected takeoff velocity, denoting a maximal propeller disk loading condition. As this figure shows, the BPF acoustic directivity is dominated by loading noise for observer angles $75^\circ \leq \theta_o \leq 150^\circ$. Therefore, it is expected that differences in measured aerodynamic loads (i.e., thrust and torque) between the right- and left-handed propeller sets would consequently produce different noise levels.

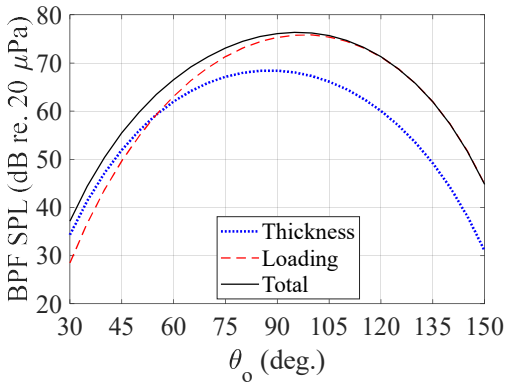

Fig. 15 Propeller BPF acoustic directivity prediction using ANOPP-PAS. *Note: $\Omega = 4800$ RPM, $V_{inf} = 75$ KEAS (high-performance takeoff condition).*

Acoustic measurement data for both right- and left-handed blade sets at expected high-performance takeoff conditions are provided in Fig. 16.

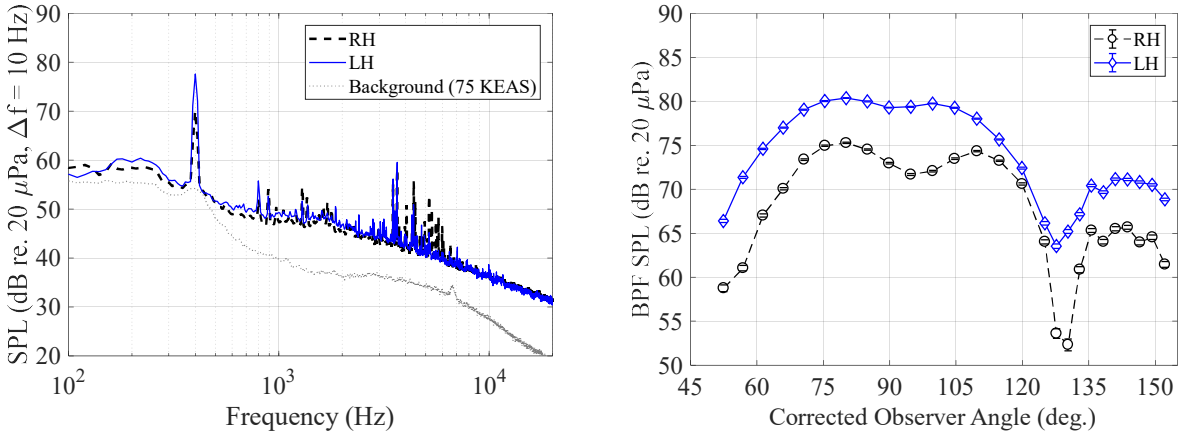

a) in-plane narrowband acoustic spectra ($\theta_c = 95°$) **b) BPF acoustic directivities**

Fig. 16 Acoustic measurement results for right- and left-handed propellers at high-performance takeoff condition.

As Fig. 16 a) shows, the two propellers have very similar acoustic spectral content; however, the left-handed propeller exhibits much higher noise levels at the BPF of 400 Hz. There are also some additional differences in higher frequency tonal content in the range of $2.5 \leq f \leq 6$ kHz between the two propellers, the source of which are discussed in the next paragraph. Furthermore, Fig. 16 b) provides the BPF acoustic directivity (400 Hz) along the entire LSAWT microphone array. The results show a consistent increase in levels for the left-handed propeller as compared to those of the right-handed one. This is believed to be attributed to the nearly 16% lower torque levels measured by the right-handed propeller as compared to the left-handed one at the same RPM. It is also worth noting that the measured BPF directivity trends of Fig. 16 b) do not compare favorably with the PAS prediction shown previously in Fig. 15. This is believed to be due to a couple of reasons. The first reason is that the predictions are based on an assumption that the blades are rigid and non-deforming. The following section provides evidence that this assumption is not accurate. Non-rigidity can result in considerable deviations in nominal acoustic behavior. The second reason is scattering and reflections present within the facility. Due to the high-speed imagery measurements that took place in this experiment and the associated lighting and support structures, there was an appreciable amount of reflective surfaces in the facility that otherwise would not be present. Despite these issues, however, it is believed to be appropriate to draw approximate conclusions on a comparative basis of the acoustic results.

We provide an overview of noise source localization results performed using the ACAM 120 on the left-handed propeller at the high-performance takeoff condition in Fig. 17. Several frequencies were selected for interrogation based on the narrowband acoustic spectra acquired using the LSAWT linear microphone array, the in-plane measurement of which is reproduced in Fig. 17 a). Beamforming images at two 1/3rd octave band center frequencies are provided in Fig. 17 b) at 2 kHz and c) 10 kHz, respectively. The first of these images shows the root region of the advancing propeller blade as the dominant noise source, with a secondary source region at the aft region of the PTS vertical support strut. A similar result is shown in Fig. 17 c) at 10 kHz, however with the dominant noise region indicated to be centered along the midspan region of the advancing propeller blade. The physical source of noise for these beam maps is believed to be due to self-noise generated by the boundary layer and resulting pressure scattering off the blade trailing edge regions. The noise at 2 kHz is more likely due to boundary layer separation noise, which is more common to inboard regions of propeller and rotor blades. The exact cause of the secondary noise sources at the PTS strut are currently unknown, however are likely due to either reflections and/or turbulent interactions with the propeller wake. Finally, Fig. 17 d) and e) show beamforming images at discrete frequencies of 3.65 and 4.375 kHz, respectively. These frequencies were selected because they contain appreciable tonal energy in the narrowband spectrum in Fig. 17 a). The beamforming images show that rather than being due to the propeller blades, the noise appears to originate from the spinner region of the propeller assembly. This could be due to the array of fasteners around the circumference of the spinner, as well as the air gap between the spinner trailing edge and propeller hub attachments. These results are very useful because they reveal noise sources associated with the propeller blades and associated flight hardware, allowing the development of possible future noise reduction technologies.

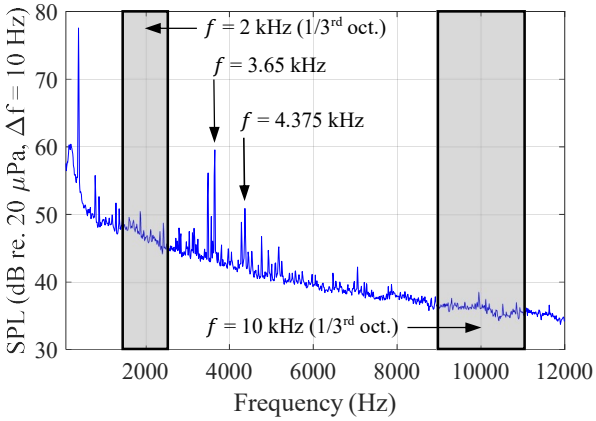

a) In-plane narrowband spectrum

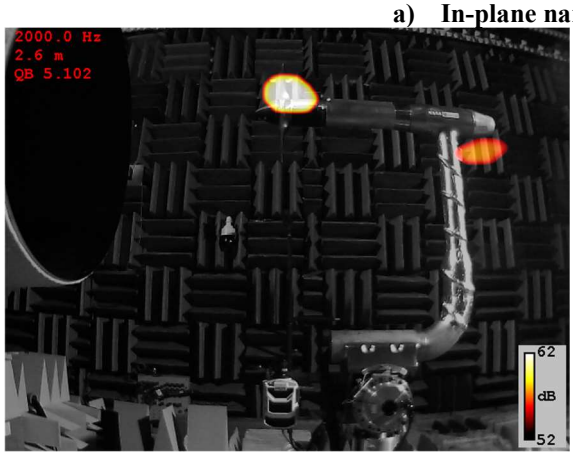

b) 2 kHz (1/3rd octave band)

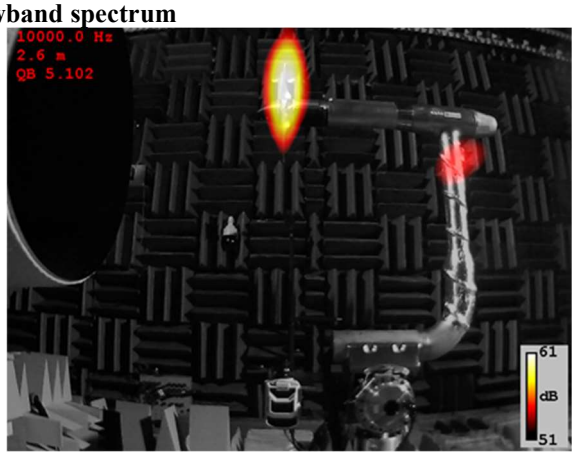

c) 10 kHz (1/3rd octave band)

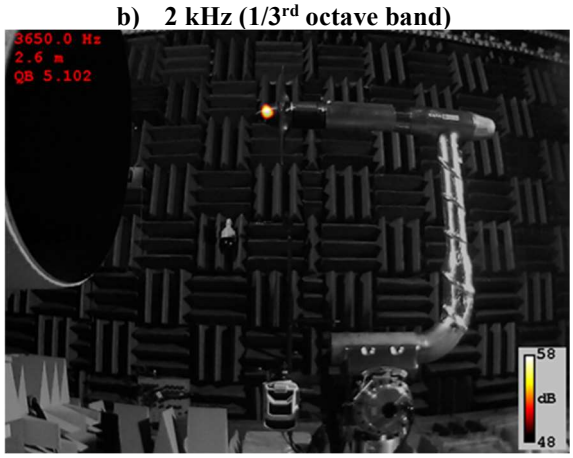

d) 3.65 kHz (narrowband)

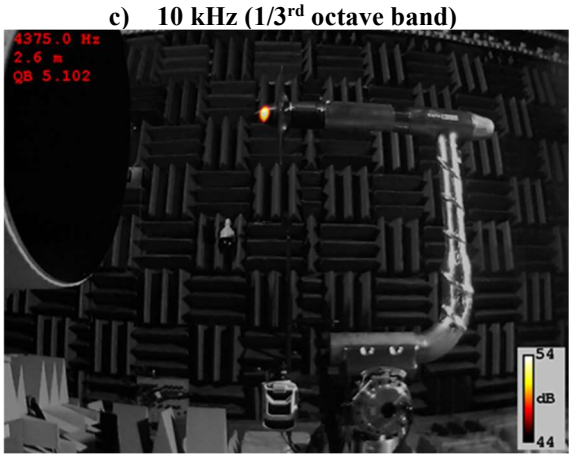

e) 4.375 kHz (narrowband)

Fig. 17 Acoustic beamforming results on the left-handed propeller at high-performance takeoff condition: a) in-plane acoustic spectrum, b) – e) beamforming maps at indicated frequencies.

3. Propeller Dynamics and Stability

Another purpose of this test was to identify any adverse operating conditions that might be present in the expected operational range of the high-lift propellers. We exposed the propellers to several dynamic events and potentially unstable conditions including deployment, stowing, yawing, and windmilling at different tunnel and propeller speeds. In these tests, we yawed rather than pitched the propeller because the high-lift propeller assembly is axisymmetric and the PTS has a smaller translation in yaw than in pitch, which helped maintain the high-lift propeller assembly in the

core tunnel flow. We monitored the remote video feeds and aft-mounted accelerometer data constantly during the tests to ensure that any potential instability that began to present in the assembly could quickly be identified and the PTS could be put into a safe condition. Throughout the tests, the high-lift propeller demonstrated smooth deployment and stowing over multiple cycles and showed little wear even after over 15 hours of collective runtime. A progression of a folding high-lift propeller deployment is provided in Fig. 18. The folding propellers also showed resilience to instability while operating through a yaw transition under multiple freestream speeds and even while yawed and windmilling at the same time. High-speed video of each of these events showed that the folding high-lift propeller blade tips were very stable and routinely traced a consistent path around the nacelle.

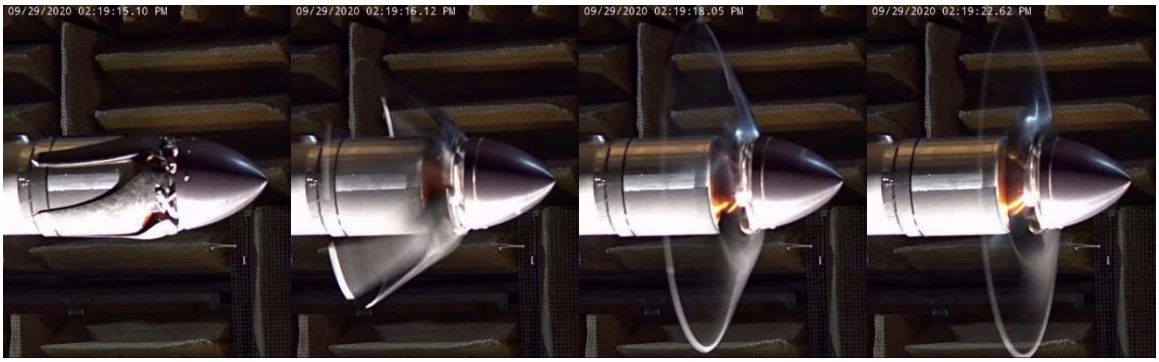

Fig. 18 A sample deployment progression of the right-handed propeller at 90 KEAS.

During each propeller runup to test speeds, we observed two potentially adverse operating conditions at or near 640 RPM and 1280 RPM when the accelerometer readouts would show a moderate but stable amplitude oscillation in Z-direction (torque) moments. The amplitude of these oscillations was greater at the 640 RPM point than at 1280 RPM and would gradually increase and then decrease in the range of around +/- 50 to 100 RPM of the points. These conditions were designated as "keep-out" zones and we would quickly pass through these speeds on the way to idle. We initially thought that these propeller speeds corresponded to the 5-per-revolution and 10-per-revolution frequencies of the folding high-lift propeller flapping mode estimated at 2 to 3 Hz. Late in the test schedule, we decided to capture high-speed video of the propeller at the smaller amplitude 1280 RPM condition to see if we could observe any blade oscillation or deflection in the hardware, but none was found. After conferring with the X-57 Aeroelastics team, these frequencies did not match those of an updated blade flapping mode analysis, and our current assumption is that these were modes of the PTS assembly. Because we cannot definitively say that these propeller speeds do not represent an adverse operating condition on the Mod IV aircraft, the high-lift propeller schedule idle speed was increased from 1200 RPM to 1500 RPM to lessen any potential risks to personnel and the aircraft from operating at these speeds.

C. High-Speed Imagery and Video

We were able to capture high-resolution, high-speed videos of the propeller in operation throughout the tests. These videos provide a means of measuring the high-lift propeller blade position to great accuracy as well as a method of identifying any potential propeller instabilities or blade deviation. We captured the raw video at 3000 frames per second with an 80 μs exposure per frame which allowed us to capture multiple test events (steady or dynamic) on the same memory buffer at once. At a propeller speed of 4800 RPM, this means that a frame is captured every 9.6° of rotation and each exposure accounts for only 2.3° of rotation. At one point, we successfully tested capturing video at nearly 16000 frames per second, and, although this filled the camera's memory almost immediately, the propeller rotating at over 5200 RPM showed smooth travel and very little blurring without adjusting the test section lighting.

Because we captured images at such a high rate throughout the tests, we could choose target points on the spinner, hub, blades, and nacelle to align the propeller to the same azimuthal position and export screenshots. We then stacked these images in post-processing to create a digital multiple exposure that enabled us to both qualitatively examine and accurately measure the effects of propeller loading and speed on an individual blade, including blade flex and tip position. For example, Fig. 19 demonstrates the effects of increasing propeller speed (or decreasing advance ratio) at a fixed freestream air speed. The blade position at zero torque is dominated by the inertial forces on the blade and exhibits a more negative coning angle and as propeller speed increases the blade is more highly loaded and therefore

travels and flexes forward resulting in a less negative angle. The effects of increasing advance ratio with greater freestream air speeds at a fixed propeller speed are shown in Fig. 20. In these images, we see that the blade becomes less loaded as freestream speed increases and the blades begin to relax and decrease the coning angle to be slightly more negative.

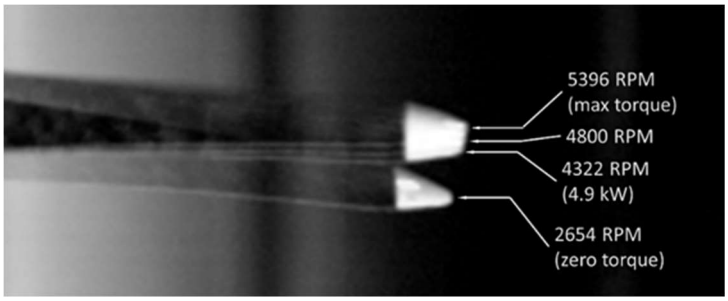

a) Right-handed propeller blade deflection vs. RPM

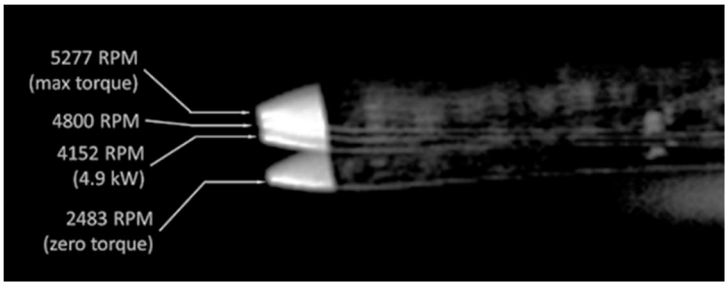

b) Left-handed propeller blade deflection vs. RPM

Fig. 19 High-speed video composite images show the effects of rotational speed at 75 KEAS.

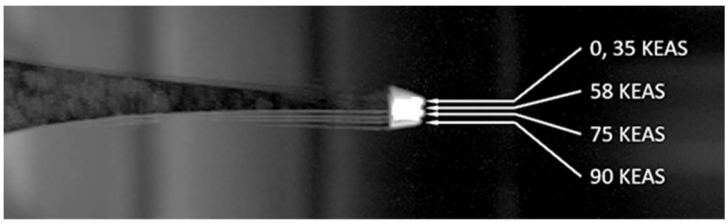

a) Right-handed propeller blade deflection vs. V_{inf}.

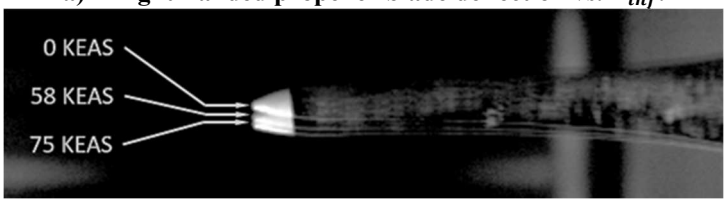

b) Left-handed propeller blade deflection vs. V_{inf}.

Fig. 20 High-speed video composite images show the effects of freestream speed at 4800 RPM.

VI. Conclusions and Future Work

In this test, we evaluated the performance and acoustics of the X-57's high-lift propellers and identified and informed the Project of two potentially adverse operating conditions discovered during the test. We also observed the assembly through several dynamic events to gain insight into the operation and behavior of folding, conformal propellers and found that the propellers performed generally as expected and exhibited smooth deployment and stowing behavior.

We found that the modified effective high-lift propeller BEM model predicted the performance of the heavier left-handed propeller quite well, and, although the PTS thrust measurements varied considerably due to load cell cross-loading, the trends in thrust still seemed to follow the BEM model. Fortunately, the PTS load cell torque data was very reliable throughout the test, and we used these values for comparison between the right- and left-handed propellers. These comparisons showed that the right-handed propeller exhibited diminished performance with respect to both the left-handed version and predictive models. The right-handed blades weighed approximately 5% less on average than the left-handed blades, and because laser scans indicated both geometries were nearly identical, the cause of the performance and weight discrepancy is likely from material property differences resulting from variations in the manufacturing process between the two blade batches. Furthermore, the acoustic data between the right and left versions validate the difference in torque by demonstrating a higher perceived sound level in the left-handed propeller at a particular blade passage frequency indicating higher blade loading.

We also found that the folding, conformal high-lift propellers were very stable throughout all test cases and dynamic events. The team constantly monitored the system health by watching live remote video of the propeller and displays of the aft-mounted accelerometer during operation for any indication of potential destabilizing or unstable conditions. At no point during the test did the propeller exhibit operational instabilities, even when some test points specifically attempted to perturb the blades from their stable positions, and both left- and right-handed propellers demonstrated smooth deployment and stowing under all freestream conditions. We also observed no blade or propeller assembly wobble on any of the high-speed video captures over the range of steady-state and dynamic events. However, we did identify two potentially adverse operating conditions for the high-lift propellers at 640 RPM and 1280 RPM where there was a moderate but stable oscillation in the accelerometer data. High-speed imagery indicated no observable blade or hardware oscillations that would produce such an effect, and the X-57 Aeroelastics team confirmed that these do not correspond to the predicted propeller blade flapping frequencies. Because we cannot definitively rule that these propeller speeds are truly free of risk, we opted to raise the X-57 high-lift propeller schedule idle speed from 1200 RPM to 1500 RPM to avoid operating at propeller speeds where the oscillations presented.

We also leveraged high-speed video to assess the propellers' dynamic behavior under a variety of conditions and created digital multiple exposure images that enabled the evaluation of propeller loading effects on blade position and bending. These videos showed that the folding propeller blades deploy as predicted in simulations and very quickly stabilize after startup. The comparative images demonstrate that the thin, outer blade sections are prone to slight bending under high blade loading and that the inertial forces tend to dominate, particularly at lower propeller speeds.

A companion test to assess the X-57 high-lift propeller stability characteristics has been proposed and is expected to be completed soon. This proposed test seeks to deflect the propeller blades from their equilibrium positions under rotation and to measure the blade hinge damping derivatives as the blades return to the equilibrium position. The results of the test will be used to improve existing folding high-lift propeller stability models. We also plan to perform a bending and torsion test of the blades used in this performance test to determine if there are any easily measurable and verifiable differences in the material properties between the right- and left-handed blades. Finally, a follow-up performance test is planned to be conducted in the LSAWT under similar conditions in which both right- and left-handed propeller blades are from the same production batches and are closely matched in weight. This test will determine if the differences in blade weight and manufacturing process caused the performance discrepancy or if there is an unidentified source of the discrepancy.

Acknowledgments

The authors wish to thank NASA's Aeronautics Research Mission Directorate for their support of this effort. The X-57 design effort is currently funded under the X-57 subproject of the Flight Demonstrations and Capabilities Project within the Integrated Aviation Systems Program, after being incubated in the Convergent Aeronautics Solutions Project within the Transformative Aeronautics Concepts Program. Several of the design tools used in this study were largely funded under the Transformational Tools and Technologies Project within the Transformative Aeronautics Concepts Program. Testing with the Propeller Test Stand was performed under the Revolutionary Vertical Lift Technology Project. The high-lift propeller detailed design and hardware fabrication was performed by Empirical Systems Aerospace, Inc. The Propeller Test Stand was designed and built by ViGYAN, Inc. The authors also wish to thank John Swartzbaugh, Stan Mason, Bryan Lamb, Mick Hodgins, and Jeff Collins for their support of LSAWT operations and Sandra Gibbs and Mark Knopp for their support of high-speed video captures and photography.

References

[1] N. K. Borer, M. D. Patterson, J. K. Viken, M. D. Moore, J. Bevirt, A. M. Stoll and A. R. Gibson, "Design and Performance of the NASA SCEPTOR Distributed Electric Propulsion Flight Demonstrator," in *16th AIAA Aviation Technology, Integration, and Operations Conference*, American Institute of Aeronautics and Astronautics, AIAA 2016-3920.

[2] B. L. Litherland and J. M. Derlaga, "A Performance Analysis of Folding Conformal Propeller Blade Designs," in *AIAA Aviation 2019 Forum*, AIAA 2019-3676.

[3] M. D. Patterson, N. K. Borer and B. German, "A Simple Method for High-Lift Propeller Conceptual Design," in *54th AIAA Aerospace Sciences Meeting*, American Institute of Aeronautics and Astronautics, AIAA 2016-0770.

[4] B. L. Litherland, M. D. Patterson, J. M. Derlaga and N. K. Borer, "A Method for Designing Conforming Folding Propellers," American Institute of Aeronautics and Astronautics, AIAA 2017-3781.

[5] M. Drela and H. Youngren, "XROTOR User Guide," 2003. [Online]. Available: http://web.mit.edu/drela/Public/web/xrotor/. [Accessed 10 1 2020].

[6] "OpenVSP," [Online]. Available: http://openvsp.org/. [Accessed May 2020].

[7] W. M. Chan, S. A. Pandya, S. E. Rogers, J. C. Jensen, H. C. Lee, D. L. Kao, P. G. Buning, R. L. Meakin, D. A. Boger and S. M. Nash, "Chimera Grid Tools User's Manual, v.2.2," 2018. [Online]. Available: https://www.nas.nasa.gov/publications/software/docs/chimera/index.html. [Accessed 10 5 2020].

[8] R. Nichols, R. Tramel and P. Buning, "Solver and Turbulence Model Upgrades to OVERFLOW 2 for Unsteady and High-Speed Applications," in *24th AIAA Applied Aerodynamics Conference, Fluid Dynamics and Co-located Conferences*, San Francisco, CA, AIAA 2006-2824.

[9] R. H. Nichols and P. G. Buning, "User's Manual for OVERFLOW 2.3, v.2.3," 2019. [Online]. Available: https://overflow.larc.nasa.gov/users-manual-for-overflow-2-3/. [Accessed 10 5 2020].

[10] A. K. Henrick, T. D. Aslam and J. M. Powers, "Mapped weighted essentially non-oscillatory schemes: Achieving optimal order near critical points," *Journal of Computational Physics,* vol. 207, pp. 542-567, 2005.

[11] R. Tramel, R. Nichols and P. Buning, "Addition of Improved Shock-Capturing Schemes to OVERFLOW 2.1," in *19th AIAA Computational Fluid Dynamics*, American Institute of Aeronautics and Astronautics, AIAA 2009-3988.

[12] F. R. Menter, "Two-equation eddy-viscosity turbulence models for engineering applications," *AIAA Journal,* vol. 32, pp. 1598-1605, 8 1994.

[13] M. L. Shur, M. K. Strelets, A. K. Travin and P. R. Spalart, "Turbulence Modeling in Rotating and Curved Channels: Assessing the Spalart-Shur Correction," *AIAA Journal,* vol. 38, pp. 784-792, 2000.

[14] R. Langtry and F. Menter, "Transition Modeling for General CFD Applications in Aeronautics," in *43rd AIAA Aerospace Sciences Meeting and Exhibit*, American Institute of Aeronautics and Astronautics, AIAA 2005-522.

[15] R. Jain, "CFD Performance and Turbulence Transition Predictions on an Installed Model-scale Rotor in Hover," in *55th AIAA Aerospace Sciences Meeting*, AIAA 2017-1871.

[16] R. Jain, "Hover Predictions on the S-76 Rotor with Tip Shape Variation Using Helios," *Journal of Aircraft,* vol. 55, pp. 66-77, 2018.

[17] "Creo Parametric 3D Modeling Software," PTC, [Online]. Available: https://www.ptc.com/en/products/cad/creo/parametric. [Accessed 19 May 2020].

[18] N. Borer and M. Patterson, "X-57 High-Lift Propeller Control Schedule," in *AIAA Aviation 2020 Forum*, AIAA 2020-3091.

[19] National Aeronautics and Space Administration, "Low Speed Aeroacoustic Wind Tunnel," [Online]. Available: https://aab.larc.nasa.gov/facilities/lsawt/. [Accessed 19 May 2020].

[20] ViGYAN, Inc., "NASA Propeller Test Stand (PTS) Manual, NNX16CLO2C," 2019.

[21] ATI Industrial Automation, "ATI Industrial Automation: F/T Sensor Mini85," 2021. [Online]. Available: https://www.ati-ia.com/products/ft/ft_models.aspx?id=Mini85. [Accessed 12 9 2020].

[22] Dimension Engineering, "DE-ACCM3D2 Buffered +/-2g Tri-axis Accelerometer," [Online]. Available: https://www.dimensionengineering.com/datasheets/DE-ACCM3D2.pdf. [Accessed 19 5 2021].

[23] Bruel & Kjaer, "Product Data, 1/4" Free-field Microphone - Type 4939," 2008. [Online]. Available: https://www.bksv.com/media/doc/Bp1851.pdf. [Accessed 06-02-2021].

[24] OPTINAV, "OptiNav BeamformX Acoustic Array System with the SIG ACAM 120," 2016. [Online]. Available: https://www.optinav.com/beamformx-aeroacoustic-detector. [Accessed 21 May 2021].

[25] Vision Research, "Phantom V12.1," 2008. [Online]. Available: http://www.adept.net.au/cameras/visionresearch/pdf/PhantomV121.pdf. [Accessed 05 2021].

[26] Vision Research, "Phantom v1610 Web Data Sheet," 2011. [Online]. Available: http://www.adept.net.au/cameras/visionresearch/pdf/PhantomV1210-v1610.pdf. [Accessed 05 2021].

[27] G. Brelsford, J. Davis, B. Kenworthy, K. Lukacovic, A. Miranda and M. Nguyen, "NASA X-57 Conformal Propeller Study," California Polytechnic State University; Empirical Systems Aerospace, 2018.

[28] L. V. Lopes and C. L. Burley, "ANOPP2 User's Manual, Version 1.2," NASA Langley Research Center, NASA/TM-2016-219342.